Post-fabrication Voltage Controlled Resonance Tuning of Nanoscale Plasmonic Antennas

Chatdanai Lumdee,[†] Seyfollah Toroghi,[†] and Pieter G. Kik[†,‡,*]

[†]CREOL, The College of Optics and Photonics and [‡]Physics Department, University of Central Florida, 4000 Central Florida Boulevard, Orlando, Florida 32816, United States

ABSTRACT

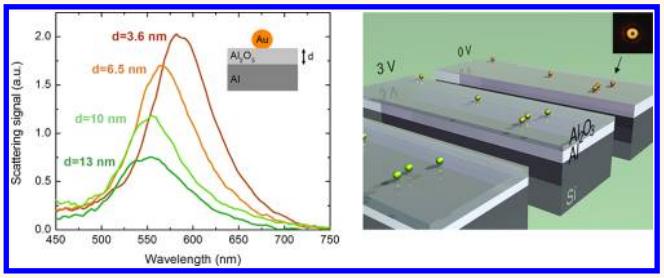

Voltage controlled wavelength tuning of the localized surface plasmon resonance of gold nanoparticles on an aluminum film is demonstrated in single particle microscopy and spectroscopy measurements. Anodization of the Al film after nanoparticle deposition forms an aluminum oxide spacer layer between the gold particles and the Al film, modifying the particle−substrate interaction. Darkfield microscopy reveals ring-shaped scattering images from individual Au nanoparticles, indicative of plasmon resonances with a dipole moment normal to the substrate. Single particle scattering spectra show narrow plasmon resonances that can be tuned from ∼580 to ∼550 nm as the anodization voltage increases to 12 V. All observed experimental trends could be reproduced in numerical simulations. The presented approach could be used as a general postfabrication resonance optimization step of plasmonic nanoantennas and devices.

KEYWORDS: plasmon resonance tuning · anodization · image dipole · gold nanoparticle · aluminum · single particle spectroscopy

Nanoscale optical antennas that support localized surface plasmon resonances are receiving a tremendous amount of attention because of their ability to produce large optical field enhancement and extreme field confinement. Localized surface plasmon resonances of nanoscale metallic structures enable a broad range of applications and effects, including surface-enhanced raman spectroscopy (SERS),[1,2] plasmon-enhanced nonlinear refraction and absorption,[3,4] plasmon-enhanced harmonic generation and frequency mixing,[5−7] plasmon-enhanced biochemical sensing,[8,9] plasmon-enhanced internal photoemission,[10−12] and plasmon-enhanced photovoltaics.[13,14] The response of nanoscale optical antennas can be engineered through a choice of material, size, shape of the structure, and the local environment.[15,16] For nanoantennas that are to be used predominantly in a fixed environment (*e.g.*, in an aqueous solution), this leaves little room for control of the antenna response after fabrication: once established the antenna composition, size, and shape are not easily modified. Here we present a method to modify the resonance response of nanoscale antennas after fabrication through substrate controlled resonance tuning.

It is well-known that a polarizable substrate can affect localized plasmon resonances of metal nanoparticles. Early work by Kuhn provided a theoretical description of the interaction between a metal surface and molecular emitters, showing a distance-dependent emission lifetime and quantum yield due to interaction of the dipole with induced image charges in the metal, as well as a small emission wavelength shift.[17] Shortly thereafter Antoniewicz demonstrated theoretically that a point dipole near a metal surface exhibits an increased effective polarizability.[18] In subsequent theoretical work by Takemori *et al.*[19] and Ruppin,[20] it was shown that similar effects occur in the coupling between a metal nanoparticle and a metal substrate. In particular the presence of the metal substrate was shown to cause a redshift of the particle-related absorption spectrum as a result of dynamic image charges. More recently, several experimental studies demonstrated plasmon resonance shifts of metal nanoparticles on a variety of substrates,[21−30] and wavelength shifts as large as few hundred nanometer were observed. However, in all these studies the particle resonance was fixed once the particles were placed on the substrate, and no further resonance control was attempted after particle deposition.

* Address correspondence to kik@creol.ucf.edu.

Received for review April 20, 2012 and accepted June 25, 2012.

Published online June 25, 2012
10.1021/nn301742p

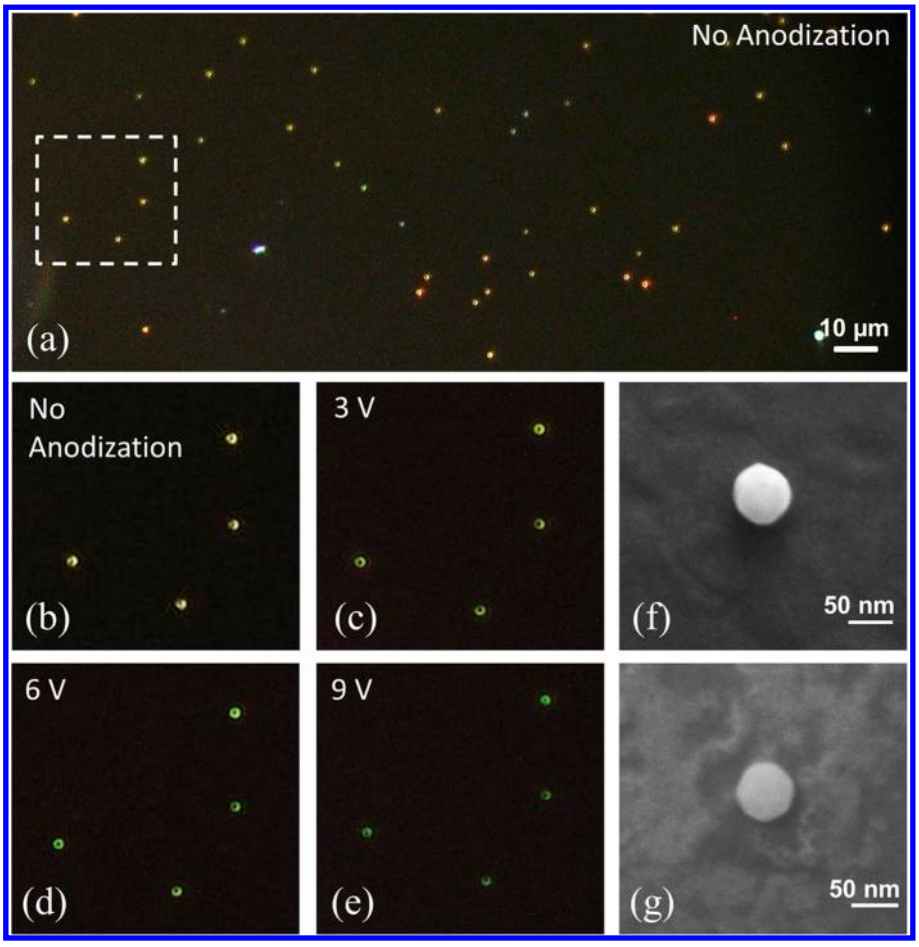

Figure 1. Darkfield microscopy images of 60 nm diameter gold nanoparticles on an aluminum substrate prior anodization (a and b), and after anodization at different voltages (c to e). Scanning electron microscopy images of Au nanoparticles before (f) and after (g) anodization.

In the present study we demonstrate postdeposition control of the localized plasmon resonance of individual gold nanoparticles on an aluminum film. Anodization of the aluminum film enables the growth of a stable aluminum oxide (Al_2O_3) film[31] that acts as a chemically controlled spacer layer between the Au nanoparticles and the Al film. Using single-particle scattering spectroscopy we track the plasmon resonance response of a set of individual deposited nanoparticles after several anodization steps, and demonstrate that the variable spacer layer thickness enables precise control of the nanoparticle resonance frequency. The method appears to leave the Au particles unaffected. While this work considers spherical gold nanoparticles, the presented approach could enable *in situ* or postfabrication optimization of a wide variety of more complicated nanoantenna structures, provided that the antenna material is not affected by the anodization process. The observed precise resonance frequency control could enable new systematic studies of light-matter interactions at the nanoscale.

RESULTS AND DISCUSSION

Figure 1a shows a real-color dark-field microscopy image of 60 nm Au particles deposited from a colloidal solution onto a 100 nm thick as-deposited Al film with a 3.6 nm thick native Al_2O_3 layer. The image shows many individual scatterers that are well separated, enabling single particle spectroscopy. All scatterers exhibit similar brightness and color, suggesting that these correspond to single Au nanoparticles that were deposited from the colloidal solution. This is further confirmed by the corresponding scattering spectra described below. Close inspection of the image shows slight color variations among the particles, possibly indicating small differences in local environment, for example, surface roughness of the deposited Al, variations in native oxide thickness, small size and shape variations (*e.g.* faceting) of the particles, or irregular deposition of surfactants from the colloidal solution. The partly inhomogeneous nature of the scattering response of supported nanoparticles would lead to artificially broadened resonance lines in ensemble measurements, highlighting the need for single-particle measurements. All particles produce a ring-shaped image under the microscope. Such ring-shaped images were also observed in prior experiments conducted by Mock *et al.*[27] and Hu *et al.*[28] on noble metal particles near a gold surface. This intensity pattern is indicative of a

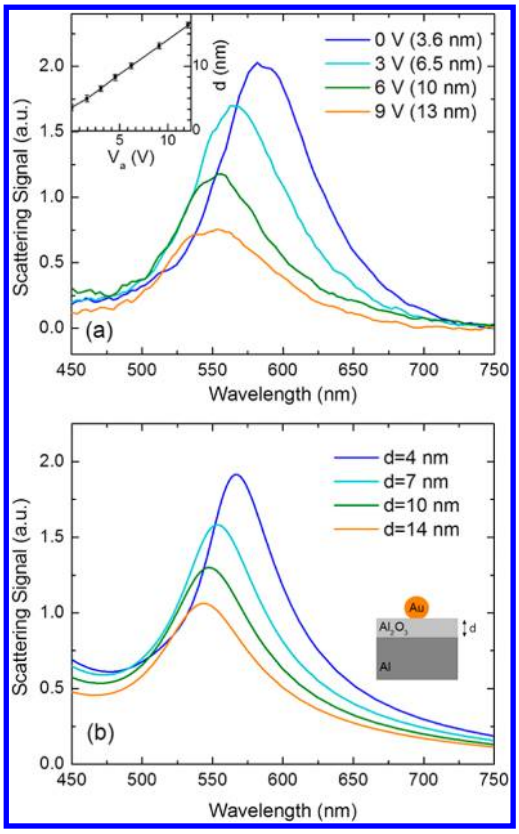

Figure 2. (a) Scattering spectra from a single Au nanoparticle for different anodization voltages. The corresponding oxide thicknesses are shown in parentheses. The inset shows the measured Al_2O_3 thickness as a function of anodization voltage. (b) Calculated scattering spectra of 60 nm Au nanoparticles on an Al_2O_3-coated aluminum film as a function of Al_2O_3 thickness *d* corresponding to the thickness values in panel a. The sample structure is shown schematically.

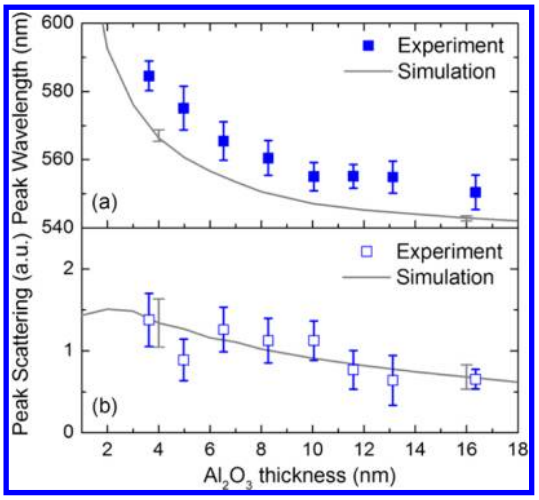

Figure 3. (a) Measured z-polarized plasmon resonance wavelength and (b) the corresponding peak scattering signal of 60 nm diameter Au nanoparticles on an oxidized aluminum as a function of Al_2O_3 thickness. The solid lines represent the results from numerical simulations. The error bars on the simulated data represent predicted signal variation due to the known colloid size dispersion, see Supporting Information.

scatterer with a dipole moment that is aligned along the optical axis, that is, normal to the sample surface. This polarization will be referred to as "*z*-polarized".

Figure 1 panels b–e show darkfield microscopy images of the same four Au nanoparticles (marked by the dashed rectangle in Figure 1a) for the as-deposited sample, as well as after anodization at voltages V_a of 3 V, 6 V, and 9 V. The color of the scattered light is seen to change from yellow/orange to green as the anodization voltage increases, suggesting a controlled and gradual change in the local environment of the particles. For all voltages the scattering remains predominantly *z*-polarized. Figure 1 panels f and g show scanning electron microscopy (SEM) images of a Au nanoparticle before anodization and another Au nanoparticle after anodization, respectively. The nanoparticles show evidence of faceting, which could introduce slight variations in particle response and particle–substrate interaction.

To correlate the experimental observations with the oxide thickness, ellipsometry measurements were carried out after each anodization step. The inset of Figure 2a shows the measured Al_2O_3 thickness as a function of anodization voltage (solid circles). The data reveal a linear relationship between the Al_2O_3 thickness *d* and the anodization voltage given by d (nm) = 3.42 + $1.07V_a$. To quantify the observed color change in Figure 1b–e, single particle scattering spectra were taken of a set of nanoparticles for all anodization voltages. Figure 2a shows representative scattering spectra for one of these particles for the as-deposited sample, as well as for three anodization voltages. All spectra show a single well-defined scattering peak with a fwhm of 70–90 nm, and a peak position in the range 550–580 nm, consistent with the expected scattering spectrum of single Au nanoparticles. As the anodization voltage is increased, two trends are observed. First, the resonance wavelength is seen to blue-shift. Second, the peak scattering signal is seen to decrease.

To quantitatively analyze the observations in Figure 2a numerical simulations were carried out as described in the Methods section. Figure 2b shows the obtained scattering spectra for 60 nm diameter Au nanoparticles on an Al_2O_3 covered Al film for four different oxide thicknesses *d* corresponding to the oxide thicknesses of the experimental data in Figure 2a. The simulated scattering spectra show remarkable agreement with the experimental data, demonstrating similar resonance wavelength, resonance shift, resonance line width, and reduction in scattering strength as the oxide thickness is increased. The simulated data exhibit a slightly higher signal at wavelengths above the plasmon resonance compared to the experimental results. This difference is due in part to the background correction procedure described in the Experimental section and the Supporting Information.

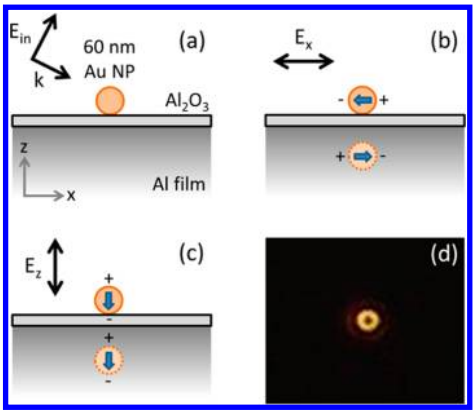

Figure 4. Schematic representation of (a) darkfield illumination of a supported Au nanoparticle on an oxidized aluminum film, (b) the particle polarization and image charge distribution resulting from *x*-polarized excitation and (c) from *z*-polarized excitation, and (d) a color image of the observed dark-field microscopy image of a Au particle on the native oxide layer on the Al film.

Figure 3a shows the measured peak wavelength position (solid squares) as a function of oxide thickness *d* obtained for a set of 10 separate particles. The error bars represent the experimental standard deviation, indicating slight spectral differences among the particles as also observed in Figure 1a. As the oxide thickness increases the average peak scattering wavelength blue-shifts from 584 to 550 nm, corresponding to a ~30 nm shift in resonance wavelength. The solid line in Figure 3a shows the simulated scattering peak position obtained by repeating the simulations in Figure 2b for several additional oxide thicknesses assuming a particle diameter of 60 nm. The simulated results reproduce the experimental trends remarkably well. On the basis of numerical simulations as a function of particle size (see Supporting Information) the known size distribution of the Au colloid could introduce peak wavelength variations of ±2 nm, as indicated by the error bars on the simulated data in Figure 3. Note that no free parameters were used in the calculation of the resonance wavelength. The experimental resonance wavelength is approximately 10 nm larger than the simulated resonance wavelength for all oxide thicknesses. This systematic difference is possibly due to slight differences between experimental and literature dielectric functions, the presence of an adventitious surface water layer,[32,33] or the presence of surface contaminants after deposition or anodization that were not considered in the simulations.

Figure 3b shows the experimentally observed peak scattering signal (open squares) as a function of oxide thickness for the same set of 10 Au nanoparticles. The error bars in the experimental data represent the standard deviation of the peak scattering signal from all particles at each oxide thickness. The scattering signal exhibits a gradual reduction as the Al_2O_3 thickness increases. The solid line shows the corresponding numerical simulation results, and the error bars on the simulated data correspond to a predicted 22% variation in peak scattering signal corresponding to the known particle size variation, see Supporting Information. The simulations exhibit a similar reduction in scattering strength as the oxide thickness is increased. This reduction in scattering strength is due in part to the frequency-dependent imaginary part of the Au dielectric function in this frequency range: as the oxide thickness increases from 3.6 to 16.3 nm, the blue-shift of the plasmon resonance leads to an increase in $\mathrm{Im}(\varepsilon_{Au})$ from 1.64 to 2.14, resulting in stronger plasmon damping for large oxide thickness.

The experimental observations can be understood in terms of the interaction of the oscillatory nanoparticle dipole moment with its dynamic image dipole in the metal substrate. Figure 4a schematically shows an Au nanoparticle on an aluminum film with an Al_2O_3 spacer under TM illumination with electric field amplitude E_{in}. At the illumination angle θ_{in} of the darkfield objective, $\theta_{in} \approx 69° \pm 2°$, the illumination contains both *x*- and *z*-polarized components. These field components in principle allow the excitation of two distinct sets of dipolar plasmon resonances and resulting image charge distributions in the Al film corresponding to *x*-polarized excitation and *z*-polarized excitation. Figure 4b schematically shows the induced horizontal (*x*-polarized) oscillation of the particle dipole moment. At frequencies well below the Al plasma frequency this dipole oscillation on the Au particle induces an oscillating image charge in the Al film with a dipole moment opposite to that of the nanoparticle. This antiparallel x-polarized dipole orientation is known to result in a redshift in the scattering spectrum compared to the response of an individual nanoparticle.[23,28,34] Figure 4c shows the corresponding situation for *z*-polarized excitation of the particle. In this case, the induced dynamic image dipole is parallel to that of the nanoparticle, again leading to a redshift of the resonance. The longitudinal near-field interaction between dipoles is known to be twice as strong as the transverse interaction, suggesting that a stronger red-shift would be observed for the *z*-polarized mode. Since the near-field dipole−dipole interaction strength decreases rapidly as the dipole separation increases, the surface-induced red-shift is expected to reduce as the oxide thickness is increased, corresponding to the experimentally observed blue-shift for increasing oxide thickness. It should be noted that the finite polarizability of Al_2O_3 also affects the particle response. Replacing the Al_2O_3 layer by an air gap would place the particle in a lower refractive index environment, leading to an additional blueshift of ~15 nm for large particle-film separation based on numerical simulations (not shown).

Owing to the different interaction strengths for lateral and normal dipoles, the presence of both

x-polarized and *z*-polarized excitation could be expected to produce a double peak feature in the nanoparticle scattering spectra, with a different red-shift depending on the polarization. However, the experimental results show single scattering peaks and pronounced ring-shaped scattering patterns (see Figure 1a–e and Figure 4d) indicating that only the z-polarized mode is detected. The absence of the lateral oscillation mode in the scattering images and spectra can be understood by considering the charge configurations of the two oscillation modes. The vertical mode induces an image dipole that is aligned along the particle dipole (Figure 4c), effectively generating an extended dipole that can radiate into the far-field, albeit predominantly along the sample surface. The horizontal mode on the other hand induces an image dipole that is oriented antiparallel to the particle dipole, corresponding to a predominantly quadrupolar charge configuration (Figure 4b) which does not radiate effectively into the far-field for particle-image charge separations much less than $\lambda/2$. A second independent reason for the absence of the lateral dipole oscillation mode is related to the excitation efficiency. The oxide-coated reflective Al substrate affects *p*-polarized and *s*-polarized illumination components differently, leading to significant differences in lateral and normal excitation field strengths. Assuming illumination with incoherent light at an angle of 70° containing equal TM and TE contributions, the Fresnel reflection coefficients predict that the E_z excitation 30 nm above an Al surface is approximately a factor 8 stronger than the E_x excitation. We therefore attribute the absence of a clear *x*-polarized contribution in the scattering images and spectra to the combined effect of a reduced excitation efficiency and a low radiation efficiency of the *x*-polarized mode. Note that the inhomogeneous dielectric environment of the Au nanoparticles is also expected to lead to the excitation of multipolar plasmon resonances. These multipolar resonances occur at frequencies above the dipolar plasmon resonance, and are not observed in the experiments.

The results presented here unambiguously demonstrate the possibility of controlling localized plasmon resonances through substrate anodization, with an experimentally observed tuning range of ~30 nm. In the material system considered here the native oxide layer puts an upper bound on the resonance wavelength, as it sets a minimum distance between the nanoparticle and the induced dynamic image charge. The simulated resonance wavelengths for thinner oxide layers (Figure 3a) suggest that significantly larger red-shifts could be achieved in the absence of a surface oxide layer. Experiments and applications utilizing these substrate-controlled resonances will likely involve immersion of these structures in aqueous environments, which is expected to result in an additional red-shift, reduced resonance line width, and improved field enhancement for spherical Au nanoparticles. Finally, the experiments involved Au nanoparticles that are thought to be only weakly bound to the sample surface. The fact that several anodization steps could be carried out without apparent degradation of the electromagnetic response of the nanoparticles and without detaching a majority of the particles suggests that the method shown here could be used to tune the resonance response of a wide variety of plasmon resonant nanoantenna structures, provided that the antenna material is not affected significantly by the anodization process.

CONCLUSION

Plasmon resonance control of 60 nm diameter Au nanoparticles supported on an aluminum film is demonstrated through substrate anodization, resulting in the formation of a thin Al_2O_3 spacer layer between the Au nanoparticles and the Al substrate. The Au nanoparticles produce ring-shaped scattering images in dark-field microscopy, indicative of *z*-polarized plasmon resonances. Single-particle scattering spectra show a consistent blue-shift of the plasmon resonance and a gradual drop in the scattering signal strength as the Al_2O_3 thickness is increased. The observations are explained in terms of oxide thickness dependent coupling between the nanoparticle and a dynamic image charge distribution in the substrate. The experimental results and numerical simulations show remarkable agreement. The presented approach could be used for postfabrication plasmon resonance optimization in a wide variety of plasmonic nanoantenna structures. The technique is simple, controlled, and could be useful for several applications that rely on plasmonic nanoantennas such as SERS, plasmon enhanced photoemission, and biodetection through observation of plasmon resonance shifts.

METHODS

Experiment. Samples were prepared on a 3-in. [100] silicon wafer with resistivity >1 Ω-cm. A 100 nm thick aluminum layer was deposited onto the Si wafer using thermal evaporation at a deposition rate of 12 Å/s using an Edwards FL 400 system. After deposition, exposure to ambient conditions leads to the rapid formation of a stable native aluminum oxide layer on the sample with a typical thickness of 2–4 nm.[35,36] The Al-coated silicon wafer was cleaved into ~1 cm^2 pieces. For nanoparticle deposition, a monodispersed gold nanoparticle colloidal solution with a particle diameter of 60.4 ± 2.6 nm was used (BB International, United Kingdom). It should be noted that this size range corresponds to the vendor-specified batch-specific size histogram. The colloidal solution contains trace amounts of

citrate, tannic acid, and potassium carbonate. The colloid was diluted with ethanol to a concentration of 2×10^8 particles/mL. Approximately 4 μL of colloid was dropped on the samples using a high precision pipet and immediately dried using air flow. The ethanol diluted solution was found to wet the substrate well. This procedure was found to lead to well-separated individual particles located on the Al surface with a particle density of $\sim$1 particle/100 μm^2. The nanoparticle-coated wafer and similarly prepared reference samples without nanoparticles were subsequently anodized in a 3 wt.% ammonium tartrate solution in deionized water (>10 MΩ-cm) at room temperature using a stainless steel counter electrode at anodization voltages in the range 1.5 V $-$ 12 V. Following each anodization step the sample was rinsed in deionized water and dried using air flow. This procedure produces an amorphous barrier-type Al_2O_3 layer with a thickness that is controlled by the anodization voltage.[31,37] The oxide thickness of the reference samples after each anodization step was determined using a J.A. Woollam variable angle spectroscopic ellipsometer. Scanning electron microscopy images were obtained using a Zeiss ULTRA-55 Field emission scanning electron microscope.

Optical microscopy and single particle scattering spectroscopy measurements were carried out after the initial particle deposition as well as after each anodization step using an Olympus BX-51 reflected light optical microscope equipped with standard dark-field optics. Most particles were found to remain on the substrate after anodization. The scattering spectra of individual nanoparticles were collected using a 50$\times$ dark-field objective (Olympus MPlanFl 50$\times$ BD, N.A. = 0.80) and a multimode fiber connected to a spectrometer (Horiba Jobin-Yvon iHR320 monochromator with Synapse CCD array). The effective collection area on the sample was $\sim$20 μm^2, and the spectral resolution was 10 nm. Single particle scattering spectra $I_{sc}(\lambda)$ were obtained using the relation $I_{sc} = (I_{NP} - I_{REF})/I_{IN}$ where I_{NP} is the signal obtained from an area containing a single nanoparticle, I_{REF} is the signal collected from a nearby region without a nanoparticle, and I_{IN} is the lamp spectrum. All spectra were corrected for the detector dark current. Finally, the thus obtained single particle scattering spectra were corrected for a small remaining offset (<4% of the peak scattering signal). The detailed data collection procedure is described in the Supporting Information.

Simulations and Calculations. Scattering spectra were determined based on three-dimensional frequency domain electromagnetic simulations[38] of a unit cell structure with a lateral size of 200 $\times$ 200 nm^2. Variation of the unit cell size between 180 $\times$ 180 and 220 $\times$ 220 nm^2 was found to lead to scattering wavelength shifts smaller than 3 nm. The silicon substrate was replaced with SiO_2 (n = 1.5) due to limitations of the modeling software; however, this choice is not expected to affect the results due to the relatively large Al thickness of 100 nm. Literature data were used for the Al_2O_3,[39] Au,[40] and Al[41] dielectric functions. The structure was illuminated at an angle corresponding to the N.A. of the objective used in the experiment. The z-dipole moment μ_z of the nanoparticle was determined at each frequency from the calculated field distributions, and the scattered power of the oscillating dipole was assumed to be proportional to $|\mu_z|^2\omega^4$ with ω being the angular frequency of the dipole oscillation.[42]

Conflict of Interest: The authors declare no competing financial interest.

Acknowledgment. This work was supported by the National Science Foundation (CAREER Award No. ECCS-0644228). We thank J. A. D'Archangel and G. D. Boreman for assistance with ellipsometry measurements.

Supporting Information Available: Further details on the data collection procedure; numerical calculations of particle size-dependent scattering spectra. This material is available free of charge *via* the Internet at http://pubs.acs.org.

REFERENCES AND NOTES

1. Felidj, N.; Aubard, J.; Levi, G.; Krenn, J. R.; Hohenau, A.; Schider, G.; Leitner, A.; Aussenegg, F. R. Optimized Surface-Enhanced Raman Scattering on Gold Nanoparticle Arrays. *Appl. Phys. Lett.* **2003**, *82*, 3095–3097.
2. Jackson, J. B.; Halas, N. J. Surface-Enhanced Raman Scattering on Tunable Plasmonic Nanoparticle Substrates. *Proc. Natl. Acad. Sci. U.S.A.* **2004**, *101*, 17930–17935.
3. Kohlgraf-Owens, D. C.; Kik, P. G. Structural Control of Nonlinear Optical Absorption and Refraction in Dense Metal Nanoparticle Arrays. *Opt. Express* **2009**, *17*, 15032–15042.
4. Toroghi, S.; Kik, P. G. Cascaded Plasmonic Metamaterials for Phase-Controlled Enhancement of Nonlinear Absorption and Refraction. *Phys. Rev. B* **2012**, *85*, 045432.
5. Moran, A. M.; Sung, J. H.; Hicks, E. M.; Van Duyne, R. P.; Spears, K. G. Second Harmonic Excitation Spectroscopy of Silver Nanoparticle Arrays. *J. Phys. Chem. B* **2005**, *109*, 4501–4506.
6. Palomba, S.; Danckwerts, M.; Novotny, L., Nonlinear Plasmonics with Gold Nanoparticle Antennas. *J. Opt. A* **2009**, *11*.
7. Utikal, T.; Zentgraf, T.; Paul, T.; Rockstuhl, C.; Lederer, F.; Lippitz, M.; Giessen, H., Towards the Origin of the Nonlinear Response in Hybrid Plasmonic Systems. *Phys. Rev. Lett.* **2011**, *106*.
8. Sperling, R. A.; Rivera gil, P.; Zhang, F.; Zanella, M.; Parak, W. J. Biological Applications of Gold Nanoparticles. *Chem. Soc. Rev.* **2008**, *37*, 1896–1908.
9. Willets, K. A.; Van Duyne, R. P. Localized Surface Plasmon Resonance Spectroscopy and Sensing. *Annu. Rev. Phys. Chem.* **2007**, *58*, 267–297.
10. Word, R. C.; Dornan, T.; Konenkamp, R., Photoemission from Localized Surface Plasmons in Fractal Metal Nanostructures. *Appl. Phys. Lett.* **2010**, *96*.
11. Wang, F. M.; Melosh, N. A. Plasmonic Energy Collection through Hot Carrier Extraction. *Nano Lett.* **2011**, *11*, 5426–5430.
12. Knight, M. W.; Sobhani, H.; Nordlander, P.; Halas, N. J. Photodetection with Active Optical Antennas. *Science* **2011**, *332*, 702–704.
13. Pillai, S.; Catchpole, K. R.; Trupke, T.; Green, M. A., Surface Plasmon Enhanced Silicon Solar Cells. *J. Appl. Phys.* **2007**, *101*.
14. Atwater, H. A.; Polman, A. Plasmonics for Improved Photovoltaic Devices. *Nat. Mater.* **2010**, *9*, 205–213.
15. Chan, G. H.; Zhao, J.; Schatz, G. C.; Van Duyne, R. P. Localized Surface Plasmon Resonance Spectroscopy of Triangular Aluminum Nanoparticles. *J. Phys. Chem. C* **2008**, *112*, 13958–13963.
16. Noguez, C. Surface Plasmons on Metal Nanoparticles: The Influence of Shpae and Physical Environment. *J. Phys. Chem. C* **2007**, *111*, 3806–3819.
17. Kuhn, H. Classical Aspects of Energy Transfer in Molecular Systems. *J. Chem. Phys.* **1970**, *53*, 101–108.
18. Antoniewicz, P. R. Effective Polarizability of a Point Dipole near a Metal Surface with a Thomas-Fermi Response. *J. Chem. Phys.* **1972**, *56*, 1711–1714.
19. Takemori, T.; Inoue, M.; Ohtaka, K. Optical-Response of a Sphere Coupled to a Metal-Substrate. *J. Phys. Soc. Jpn.* **1987**, *56*, 1587–1602.
20. Ruppin, R. Optical-Absorption by a Small Sphere above a Substrate with Inclusion of Nonlocal Effects. *Phys. Rev. B* **1992**, *45*, 11209–11215.
21. Stuart, H. R.; Hall, D. G. Enhanced Dipole−Dipole Interaction between Elementary Radiators near a Surface. *Phys. Rev. Lett.* **1998**, *80*, 5663–5666.
22. Okamoto, T.; Yamaguchi, I. Optical Absorption Study of the Surface Plasmon Resonance in Gold Nanoparticles Immobilized onto a Gold Substrate by Self-Assembly Technique. *J. Phys. Chem. B* **2003**, *107*, 10321–10324.
23. Pinchuk, A.; Hilger, A.; von Plessen, G.; Kreibig, U. Substrate Effect on the Optical Response of Silver Nanoparticles. *Nanotechnology* **2004**, *15*, 1890–1896.
24. Murray, W. A.; Suckling, J. R.; Barnes, W. L. Overlayers on Silver Nanotriangles: Field Confinement and Spectral Position of Localized Surface Plasmon Resonances. *Nano Lett* **2006**, *6*, 1772–1777.
25. Jiang, G. Q.; Baba, A.; Ikarashi, H.; Xu, R. S.; Locklin, J.; Kashif, K. R.; Shinbo, K.; Kato, K.; Kaneko, F.; Advincula, R. Signal

Enhancement and Tuning of Surface Plasmon Resonance in Au Nanoparticle/Polyelectrolyte Ultrathin Films. *J. Phys. Chem. C* **2007**, *111*, 18687–18694.
26. Knight, M. W.; Wu, Y. P.; Lassiter, J. B.; Nordlander, P.; Halas, N. J. Substrates Matter: Influence of an Adjacent Dielectric on an Individual Plasmonic Nanoparticle. *Nano Lett.* **2009**, *9*, 2188–2192.
27. Mock, J. J.; Hill, R. T.; Degiron, A.; Zauscher, S.; Chilkoti, A.; Smith, D. R. Distance-Dependent Plasmon Resonant Coupling between a Gold Nanoparticle and Gold Film. *Nano Lett* **2008**, *8*, 2245–2252.
28. Hu, M.; Ghoshal, A.; Marquez, M.; Kik, P. G. Single Particle Spectroscopy Study of Metal-Film-Induced Tuning of Silver Nanoparticle Plasmon Resonances. *J. Phys. Chem. C* **2010**, *114*, 7509–7514.
29. Du, C. L.; You, Y. M.; Johnson, K.; Hu, H. L.; Zhang, X. J.; Shen, Z. X. Near-Field Coupling Effect between Individual Au Nanospheres and Their Supporting SiO(2)/Si Substrate. *Plasmonics* **2010**, *5*, 105–109.
30. Chen, S. Y.; Mock, J. J.; Hill, R. T.; Chilkoti, A.; Smith, D. R.; Lazarides, A. A. Gold Nanoparticles on Polarizable Surfaces as Raman Scattering Antennas. *ACS Nano* **2010**, *4*, 6535–6546.
31. Diggle, J. W.; Downie, T. C.; Goulding, C. W. Anodic Oxide Films on Aluminum. *Chem. Rev.* **1969**, *69*, 365–405.
32. Haynes, C. L.; Van Duyne, R. P. Plasmon-Sampled Surface-Enhanced Raman Excitation Spectroscopy. *J. Phys. Chem. B* **2003**, *107*, 7426–7433.
33. Haes, A. J.; Van Duyne, R. P. A Nanoscale Optical Biosensor: Sensitivity and Selectivity of an Approach Based on the Localized Surface Plasmon Resonance Spectroscopy of Triangular Silver Nanoparticles. *J. Am. Chem. Soc.* **2002**, *124*, 10596–604.
34. Lal, S.; Westcott, S. L.; Taylor, R. N.; Jackson, J. B.; Nordlander, P.; Halas, N. J. Light Interaction between Gold Nanoshells Plasmon Resonance and Planar Optical Waveguides. *J. Phys. Chem. B* **2002**, *106*, 5609–5612.
35. Campbell, T.; Kalia, R. K.; Nakano, A.; Vashishta, P.; Ogata, S.; Rodgers, S. Dynamics of Oxidation of Aluminum Nanoclusters Using Variable Charge Molecular-Dynamics Simulations on Parallel Computers. *Phys. Rev. Lett.* **1999**, *82*, 4866–4869.
36. Langhammer, C.; Schwind, M.; Kasemo, B.; Zoric, I. Localized Surface Plasmon Resonances in Aluminum Nanodisks. *Nano Lett.* **2008**, *8*, 1461–1471.
37. Hutchins, G. A.; Chen, C. T. The Amorphous to Crystalline Transformation of Anodic Aluminum-Oxide during Anodization in an Ammonium Citrate Electrolyte. *J. Electrochem. Soc.* **1986**, *133*, 1332–1337.
38. *CST Microwave Studio*; Computer Simulation Technology: Darmstadt, Germany, **2011**.
39. Lichtenstein, T. *Handbook of Thin Film Materials*. University of Rochester: Rochester, NY, 1979.
40. Johnson, P. B.; Christy, R. W. Optical Constants of the Noble Metals. *Phys Rev B* **1972**, *6*, 4370–4379.
41. Palik, E. D.; Ghosh, G. *Handbook of Optical Constants of Solids*; Academic Press: Orlando; London, 1985.
42. Jackson, J. D., *Classical Electrodynamics*; Wiley: New York, 1962.